Int. J.Nano Dimens. 4(2): 117-129, Autumn 2013
ISSN: 2008-8868

Contents list available at **IJND**

International Journal of Nano Dimension

Journal homepage: *www.IJND.ir*

Accurate characteristics of Helium in nano-channels

El-Sharkawy H. A.*

Egyptian Petroleum Research Institute (EPRI), Petrochemical Department, Nasr City, Cairo. Eavpt. P.O. Box 11727.

Received: 25 July 2012
Accepted: 29 October 2012

ABSTRACT

This article describes an accurate subPico flowmeter bifurcatedin to liquid and gas flowrates less than 1mol/s for both *MEMS/NEMS* and cryogenic technology applications. The *MEMS/NEMS* are described as either two Gauges (instrument), or quartz fluctuating forks, even if the liquid or gas flows through an element, as well as cryogenic technology consisting of arrays of either parallel photonic crystal micelles or parallel rectangular nano-channels by using the lithography and anodic bonding techniques on silicon micelles. The behavior of gas or liquid Helium at high pressure was found to differ from the prediction of the conventional *Heigen Equation*. A hydro-dynamic model showed a gas or liquid properties namely molar flow rate, input and output pressure, two pressure gauges or quartz fluctuating (*Todd Helmenstine*) forksand the temperature. The measurements with fluid Helium demonstrated that the flow cells could span the flow range from 10^{-15} to 10^{-12} mol/s. This paper had focused on a versatile method of creating wide area defect free crystals based on interference lithography (MEMS/NEMS and cryostat). This technique involves splitting a monochromatic plane wave from a laser into multiple beams and recombining them inside a photoresist (fluid compressibility).

Keywords: *Nano-Flow; MacroScale Channels; Surface Effects; Navier-Stokes Equations; Super-Hydrophobicity.*

INTRODUCTION

The area of optical communication has seen rapid growth in the past few years. Considerable study has been devoted to the control of optical properties of materials through the use of photonic crystals, materials with a periodic arrangement of electric medium in one, two or three dimensions, with periodicities on the order of the wavelength of the light being manipulated. Photonic crystals can be of photonic band gaps (PBGs) where all frequencies within the gap are hidden to propagate the crystal [1].

* Corresponding author:
El-Sharkawy H. A.
Egyptian Petroleum Research Institute (EPRI), Petrochemical Department, Nasr City,
Cairo, Egypt, P.O. Box 11727.
Tel +200 111-554-10100
Fax +202-22747433
Email laereate2007@hotmail.com

In this paper, we describe the passive coherent combining of 10 diode lasers in an external cavity using the Talbot self-imaging effect. The extended-cavity simply consists of a volume Bragg grating (VBG) which acts as the external cavity output coupler, positioned at a quarter of the Talbot distance $Z_T = 2p^2/\lambda \cong 20$ mm from the laser array front facetto ensure the highest discrimination between the in-phase and the out-of-phase supermodels (see Figure 1). The VBG reflectivity is 40% at 976 nm, with a spectral bandwidth $\Delta\lambda = 0.3$ nm; its angular acceptance is $\Delta\theta = 3°$ (full width at $1/e^2$), which is larger than the divergence of the laser array in both directions after fast axis collimation [2]. Consequently, the extended-cavity laser array threshold is 0.9 A, and the output power reaches 1.7 W at the operating current of 3.9 A [3].Depending on the angle of the VBG, the extended-cavity may operate either in the *out-of-*phase or the *in*-phase array supermode.

PBG is a function of (D and R) the geometry and reflective contrast of the photonic crystal, with the phenomenon of a complete PBG only observed in medium electric contrast three dimensional photonic crystals. Several techniques aiming at converting the emission from a low fill factor coherent laser array into a single lobe have already been proposed. One can classify them into aperture-filling techniques and superposition techniques. The aim of former is to generate a uniform near field emissive area, in phase and intensity, by filling the gaps between the lasers.

The other solution consists in the superposition of the different beams from each laser by use of a diffractive optical element (DOE). Indeed, DOE are usually used to split a beam into several beams propagating at different angles corresponding to the diffraction orders of the grating [4]. A proper design of the phase profile of the DOE provides a fine control of the amplitude and phase of each diffraction order. This optical device can also be used to combine several coherent laser beams on top of one another (as shown in Figure 2).

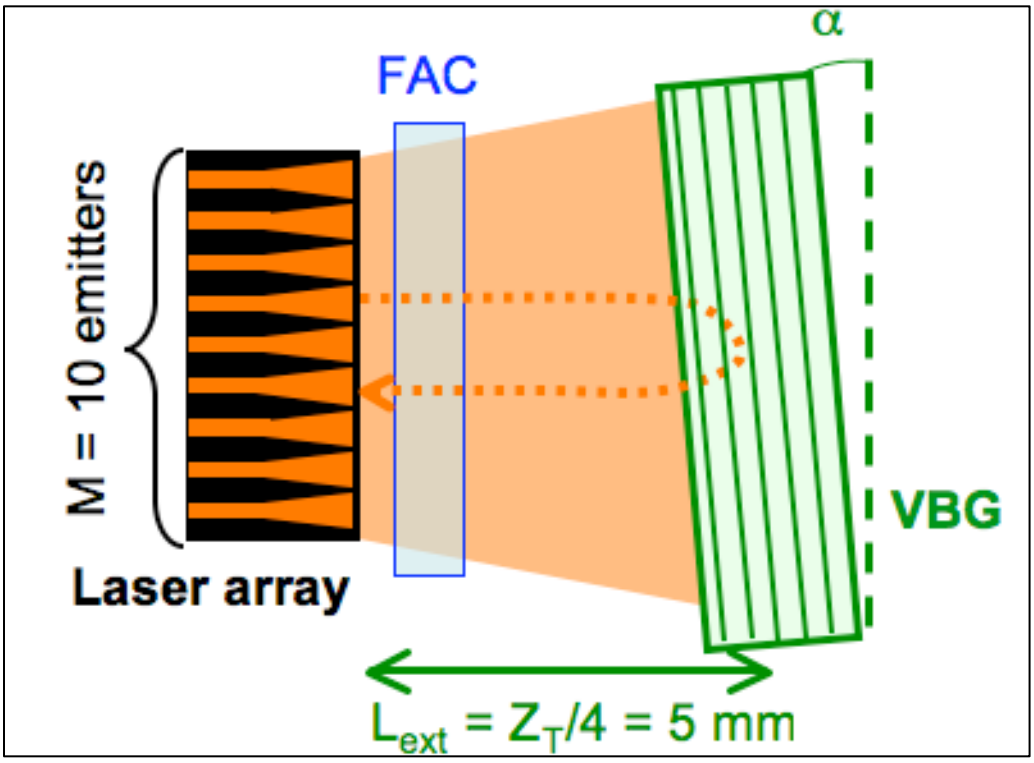

Fig. 1. Experimental setup of the Talbot extended-cavity laser array with a volume Bragg grating; FAC : fast axis collimation lens; VBG : volume Bragg grating.

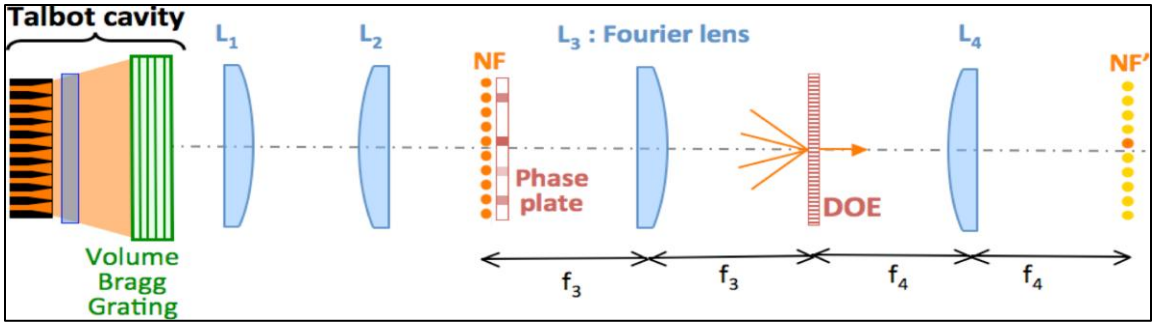

Fig. 2. Experimental setup for the coherent conversion of the array super mode; NF, NF' : near-field images; DOE :diffractive optical element; L_i (i = 1 to 4) : cylindrical lens with focal length f_i.

Herein, the extracavity coherent superposition of the 10 emitters with a DOE has an efficient conversion of the multilobed array supermode into a Gaussian-like mode, up to a power of 365 mW. This can explain the lower conversion efficiency, as compared to theory, by the low coherence of the laser array emission. The best configuration results in conversion efficiency of 83%. Experimentally, the conversion efficiency reaches 50% and is limited by the imperfect coherence of the laser array. Nevertheless, the conversion setup provides an actual measurement of the power in the selected array supermode.

The DOE has been manufactured by Holoeye Photonics according to our design; its period (a $\{0,\pi\}$ binary grating) is 488µm and the motive width is 88µm. From its diffraction pattern we deduce a diffraction efficiency of η_0 = 83 % in accordance with the theoretical value. The phase mask has been realized in our laboratory by ion etching of a BK7 plate. It consists of a phase step of $0.99\times\pi$at λ = 976 nm, and a width of 80µm. Neither the phase plate nor the DOE are antireflection coated; we evaluate the transmission of the optical system to T = 85 % [5].

The Talbot external cavity laser array is aligned in order to operate in the *out-of*-phase mode. The near field of the array is imaged with 1 focal lens (L_1) on the phase plate Φ_1, which shifts of π the phase of the 5th emitter only [6].

Figure 3 shows the near-field profiles imaged in NF' without the DOE, at the operating current I = 1A; the total power is distributed among the M = 10 emitters, and roughly follows the theoretical cosine profile. With the DOE inserted in the conversion setup, most of the optical power is within one major peak, as expected.

Coherent combination setup is described on Figure 2. It is based on a phase grating Φ_1, placed in the Fourier plane of the collimating lens L_3. The grating aims at superimposing the beams from the M emitters on one; behind the focusing lens L_4, the near-field image NF' consists in one main spot with most of the optical power.

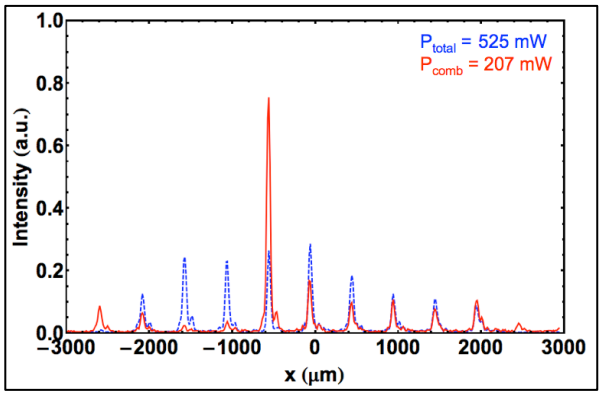

Fig. 3. Experimental slow-axis near-field profile in the plane NF' at I = 1A, without (blue dashed line) and with (red solid line) the DOE.

The beam quality factor of the combined beam has been measured to M^2 = 1.7 in the slow axis (Figure 4), close to the value of the individual emitters [7]. The ratio η of the power which is actually collected into that peak has been measured as a function of the operating current of the extended-cavity array (C): close to threshold, the combining efficiency reaches η = 50 %, and it remains above 37 % at the maximum operating current. The maximum power in the combined spot reaches 310mW at I = 1A, without correction from the T = 85% transmission of the whole setup – P_{comb} = 365mW with correction.

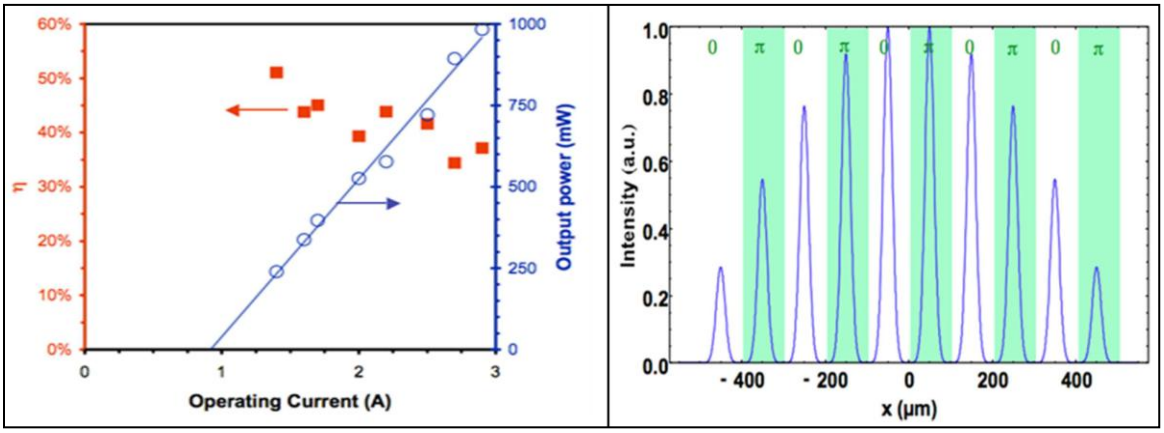

Fig. 4. Theoretical (left) and (right) intensity profiles of the near-field, with M = 10, w = 15 μm,p = 100 μm, λ = 976 nm. Evolution of experimental conversion efficiency η within the out-of-phase mode (red full square, left) and the output power of the extended-cavity laser array (blue circle, right) with the operating current.

This is significantly larger than previous results of coherent combining into one peak from an array of diode lasers [8]. The decline of η with the operating current indicates a fall in the coherence of the laser array as the output power is increased.

Indeed since only the out-of-phase supermode can be efficiently converted to a Gaussian-like mode, the overall combining efficiency is proportional to the ratio C of power which is actually in the out-of-phase supermode at the output of the extended-cavity array. This could have been predicted from the experimental far-field profile of the extended-cavity laser array, C; is between 60% and40%.

Liquid flow in micro/nano-scale channels is widely used in recently advanced micro/nano-electromechanical systems, in micro-total-analytical systems (*μTAS*). Surface effects substantially dominate the flow due to the high surface to volume ratio in micro/nano-fluidic devices [9]. The liquid Helium flow in *micro/nano-channels* becomes much more difficult than that in *macroscale channels*. However, there are very few demonstrated methods for reducing the friction of the liquid in micro/nano-flow [10].

The slip effect becomes very important in *micro/nano-scale* flow as the characteristic length decreases. In other words, the friction decrease requires the slip increase. Surface micro/nano-scale structures may enhance the surface hydrophobicity and then increase the *velocity slip* of the liquid flow at a structured surface. The effects of the surface roughness on the *micro/nano-flow boundary* conditions may be more complex due to different mechanism and most of the nano-bubbles are often in a heterogeneous cryostat, which means that there must be patches of air beneath the structure gaps. The *velocity slip* of liquid at a solid surface has been measured experimentally [8-17] and simulated by the molecular dynamics method [18-26].

The factors dominating the *liquid-solid slip* in the experimental measurements often include surface wettability [27, 28], surface roughness [29-31], shear rate [32-35] and gas films.

Originally inspired by the unique property of the pressure driven flow of a classic Newtonian fluid, such as water, in a macro-scopic container can usually be described by *Poiseuille's* law. In contrast, *do slip* and the *no-slip* boundary (arrow) for the liquid flow in merely an approximation at *macro-scale condition* is due to the high reflectivity of band gap regions. Typical photonic crystals constructed by interference lithography start out as polymer air structures and have a high reflective index contrast silicon-air photonic crystals using interference lithography. This law follows routinely from the *Bernoulli* Equation (Area = $4\pi r^2$ &Volume = $4/3\pi r^3$)together with some assumptions about the nature of fluid motion at the wall of container [36]. It is customary to assume that the tangential fluid velocity vanished at a wall, i.e., *no-slip* boundary conditions.

Bernoulli Equation is $P + (0.5)\ \rho\ V^2 + \rho\ gh$ = a constant; as well as volumetric flow rate is area times velocity. Here, P stands for pressure, ρ is the

fluid's density, V is its velocity, h is its height and g is the gravitational acceleration constant, which are9.80 m/s^2. The way to think of this intuitively (slope) is that the sum of the static pressure, the dynamic pressure and the gravitational pressure remains constant.

All flow experiments were carried out at liquid ^{4}He temperature (≃ 2.4 K), and saturation vapor pressure, = 1 bar. The pressure measurements are carried out using simultaneously two detectors and two fluctuating forks. One is located in the first reservoir up-stream of the nano-cell and the other in the second reservoir of the nano-cell.

Interestingly, the apparent breakdown *of Poiseuille's law* in more details extending the experiments to much smaller length scales as following:

(1)Designed and constructed the nano-flow measurement at low temperature for special purposes.

(2)*Poiseuille'slaw* deviations in *submicrometer channels* depend systematically on the size of the channels, walls roughness, and the properties of liquid ^{4}He (at T= 0 K, γ= 0.375±0.004dyne cm^{-1}).

(3)All deviations correspond to flow rates that are "larger" than predicted by the theory with no-slip boundary conditions. Hence, our results indicate that slip is significant, and allow us to estimate the slip length.

(4)The liquid ^{4}He flows through a bundle of hollow photonic crystal fiber (PCF) fixed between two reservoirs in which the pressures can be controlled, at desired values P_{in} and P_{out}, respectively.

It is also very important to measure the dimensions of the channel accurately because the geometrical characteristics have a great influence on the mass flow rate: for example, the analytical expression of the mass flow rate, in hydro-dynamic and *slip regimes*, is proportional to the power of the channels diameter. Therefore, the cross-sectional of the PCF were scanned by SEM FEI Nano SEM 200 and calculated the diameter for all channels. Since the length of the channel is much smaller than its diameter, even if the channel ends effects could be neglected. The friction of the channels wall is usually smaller than 1.3 nm[37].One main goal of this analysis is to identify the nature of iron sulfides in Opalinus clay stones.

EXPERIMENTAL

Experiment Setup and Data Reduction

The experimentation for this study was performed using a relatively simple but highly effective apparatus. The apparatus used was designed with the intention of conducting highly accurate pressure drop measurements. The apparatus consists of four major components. These are the fluid delivery system, the flow meter banks, the test section assembly, and the data acquisition system. An overall schematic for the experimental test apparatus is shown in Figure 5.The fluid delivery system consists of a high pressure cylinder filled with ultra high purity nitrogen in combination with a stainless steel pressure vessel. Thus, after the working fluid passes through the apparatus, it is passed into a sealed collection container. The working fluid, distilled water is stored in the stainless steel pressure vessel [38]. As the pressurized nitrogen is fed into the pressure vessel, the working fluid is forced up a stem extending to the bottom of the vessel, out of the pressure vessel, and through the flow meter array and test section. Flow rate of the water entering the array is further regulated using a metering valve. Two Coriol is flow meters are necessary in order to accommodate different range of flow rates. Both flow meters were factory calibrated. After passing through the flow meter array, fluid enters the test section assembly. The test section assembly contains the test section as well as the equipment necessary for measurement of inlet and outlet fluid pressure drop. The test section is placed on a high density polyethylene (HDPE) sheet. Four adjustable bolts and a level were installed on the HDPE board to keep the test section in a horizontal position. For data acquisition, a National Instruments SCXI-1000 data collecting system was used [39]. All digital signals from the flow meters and pressure transducer were acquired and recorded by the Windows-based PC with the self-developed Lab View program Figure 6.With the measured data, the friction factor was calculated by:

$$F = 2\,D\,\Delta P\,/\,\rho\,LV^2$$

and the Reynolds number was calculated by

$$Re = \rho\,VD\,/\,\mu$$

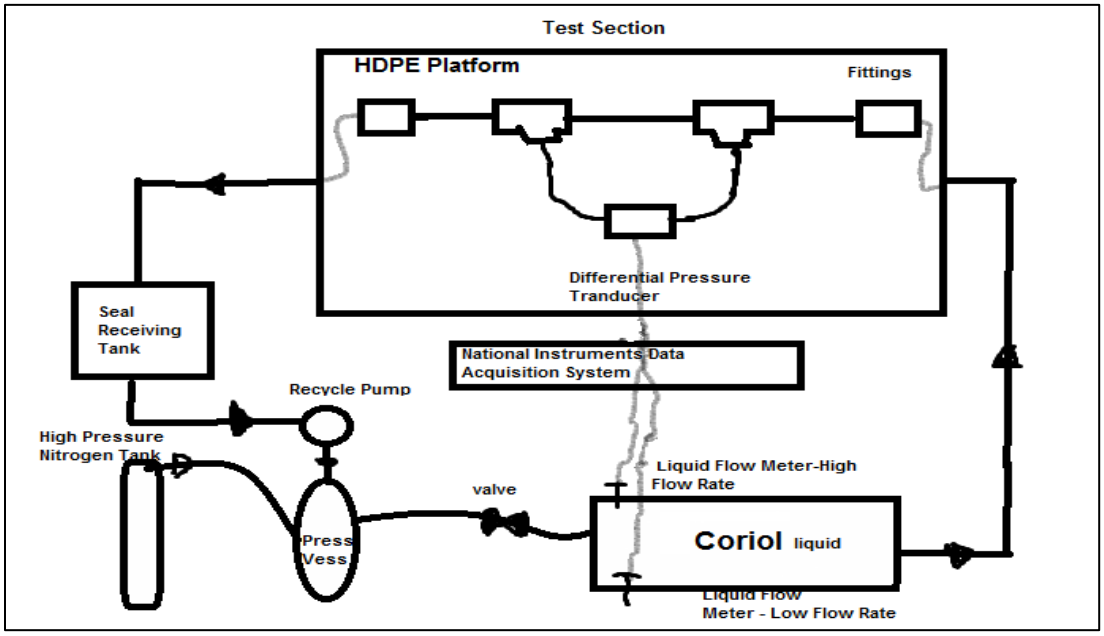

Fig. 5. Schematic diagram of pressure drop measurement system.

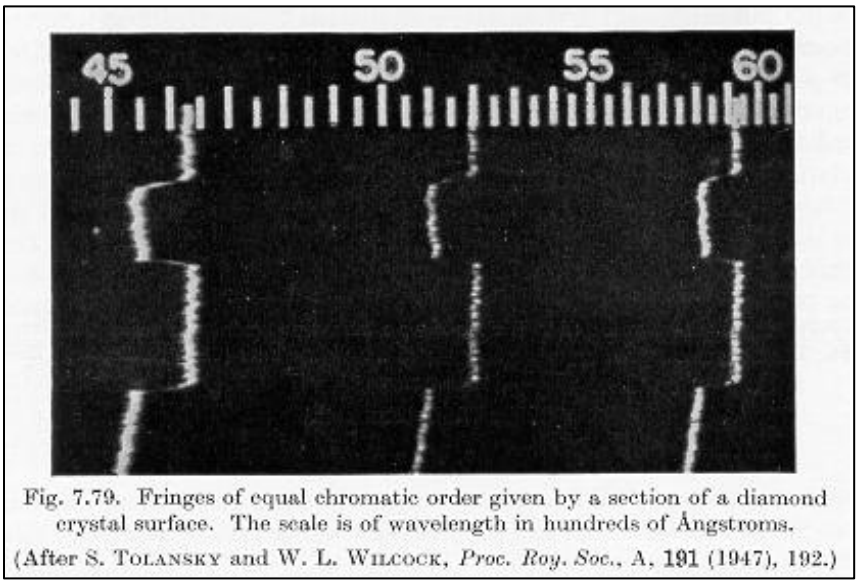

Fig. 7.79. Fringes of equal chromatic order given by a section of a diamond crystal surface. The scale is of wavelength in hundreds of Ångstroms.
(After S. Tolansky and W. L. Wilcock, *Proc. Roy. Soc.*, A, 191 (1947), 192.)

Fig. 6. An example of windows-based PC

Since $d_2 - d_1$ is proportional to $\lambda_{2,m} - \lambda_{1,m}$, the profile of the cross-section of an unknown surface is obtained by plotting a single fringe on a scale proportional to the wavelength [40].The spectroscopic slit is in effect selecting a narrow section of the interference system and each fringe is a profile of the variation of d in that section since there is exact point-to-point correspondence between the selected region and its image on the slit. Small changes in d are determined by measuring small changes in λ. There are no ambiguities as to whether a region is a hill or a valley. There are no ambiguities at a discontinuity as we would have with monochromatic light where it is difficult to determine which order belongs to

each fringe. Surface height variations in the Angstromrange can be determined.

Two disadvantages are

1) We are getting data only along a line and

2) The sample being measured must have a high reflectivity.

The dramatic implosion of the pellet generates the high-density, high-temperature environment necessary for the fusion of the pellet's deuterium and tritium and the accompanying release of an energetic neutron [41]. Researchers hope that eventually laser-induced inertial confinement fusion (ICF) will reach an ignition state, a state at which more energy is released by the fusion process than that used to produce the high-temperature, high-density conditions necessary for ICF. The problem of infrared beams' ineffectiveness is conveniently solved on the OMEGA laser system with potassium dihydrogen phosphate (KDP) crystals, which, when correctly oriented to an incoming beam, triple its frequency. KDP crystals are appropriate for OMEGA'S frequency conversion process because they convert relatively broad bandwidths of IR frequencies to the UV [42]. Generation of the third harmonic frequency (see Figure 7), which is used for the OMEGA system, involves at least two KDP crystals, a "doubler" and at least one "tripler." The doubler crystal splits the incoming laser beam into components polarized along each of the crystals' two axes, the ordinary (*o*) axis and the extraordinary (*e*) axis [43]. When the beam is polarized at 35°to the doubler's *o* axis, there are two *o*-polarized photons for each *e*-polarized photon at the original frequency. One *o*-polarized photon and the *e*-polarized photon combine into one green second-harmonic photon polarized in the *e* direction. The tripler crystal(s) combine the green photon and the remaining IR *o*-polarized photon into one *e*-polarized ultraviolet photon with three times the frequency and energy of one of the three IR photons [44].Infrared beams, however, are ineffective in ICF because only a small fraction of their energy is actually absorbed by fuel pellets and, furthermore, much of the absorbed energy is diverted to "suprathermal" electrons which move through the plasma and heat the fuel before it is compressed.

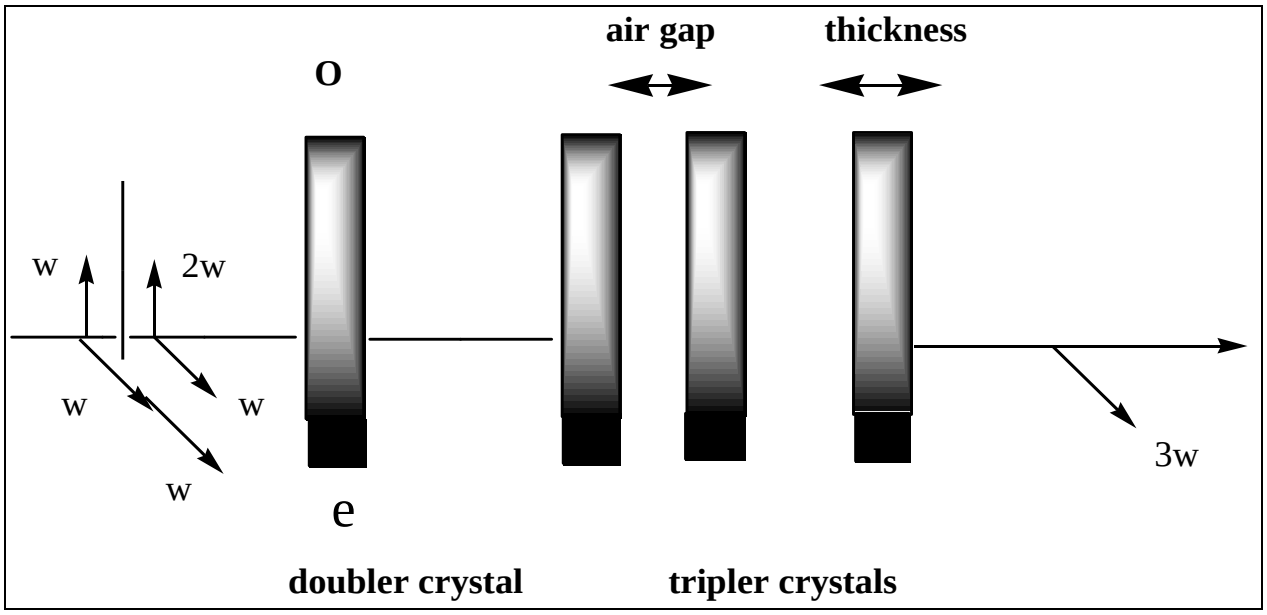

Fig. 7. Third-harmonic frequency generation with doubler and tripler crystals. Three IR photons (ω)polarized in two directions enter the doubler, and two combine to form a green photon (2ω) with twice an IR photon's frequency. The green photon and the remaining IR photon enter the tripler and combine to form a UV photon (3ω) with three times an IR photon's frequency. The air gaps between the triplers, the thicknesses of the triplers, and the tilts of the triplers affect the efficiency of this conversion at various incoming frequencies.

Experimental Section

Helium Crucibles/Scales

The present specifications for Helium (TU 51-940-80) call for the output of three grades of Helium: purified, containing not less than 99.99-99.995 % Helium; that with a total content of Helium and neon of not less than 99.99 %, and technical, containing not less than 99.8 % Helium. The specifications also stipulate the content of the large number of possible impurities in Helium-hydrogen, nitrogen, oxygen, argon, hydrocarbons, carbon dioxide and oxide, neon, and water vapor. Thus, in grade A purified Helium a bulk fraction of not less than 99.995 % is required for Helium, with a neon content of not more than 0.004 % and the content of each of the remaining impurities of not more than 0.0001-0.0005 %. At the industrial plants dependent on recovered natural gas and petroleum associated gas, Helium has been recovered from 0.05% to 0.3% ^{4}He processed. Before input to the low-temperature units, carbon dioxide, hydrogen sulfide, and organosulfur compounds are extracted by ethanolamine solutions from the gases being processed, which are thoroughly dried using molecular sieves. Silica gel was used earlier at the first plants to dry gases. At all the plants the method of low-temperature condensation at the units of propane and higher hydrocarbons plant or ethane and higher hydrocarbons plant, has been used for gas processing. The oxidations of hydrogen and adsorption at the temperature of liquid nitrogen have been used for removal of impurities in the final purification of Helium. Low-temperature phenomena including mineral ordering/phase transitions and blocking/unblocking of superparamagnets. To first order we can think of terrestrial ^{3}He as primordial gas trapped in the mantle, and the much-more-abundant ^{4}He as a mixture of radiogenic crustal and primordial mantle components. Helium makes its way from the Earth's interior to the surface in various ways, and variations in the isotopic ratio provide important information bearing on internal reservoirs and transport processes [45].

ALL THE STARS IN THE NIGHT SKY are (or have been) busily burning hydrogen and producing light, heat, helium and heavier elements. Yet cosmologists tell us that the vast majority of the helium in the universe is (like helium) actually of pre-stellar origin, containing primordial nuclei forged in the first few minutes following the Big Bang, with relative numerical abundances ^{3}He: ^{4}He: H of approximately 10^{-5} : 0.1 : 1.

Here, the photonic crystal is used inside the metal waveguide as an *Aqua-Regia* Treatment. High-resistivity (greater than 104 Ω cm) silicon is chosen because the absorption is low enough to be negligible, and the reflective contrast is essentially dispersionless (n = 3.418) over the entire bandwidth of the THz pulses [46]. Coupling100% of the input waves from free space into the waveguide, so, instead of measuring the reflected beam at normal incidence, we might employ a set-up, as shown in the inset of Figure 7. This figure is best appreciated in view of the electronic web version of this article.

This literature is inevitably reviewed and varnished ^{4}He liquid flowing over a multiplex solid surface (1 μm, 2 μm, 1 μm, 500 nm). The challenge of the same thickness effect can be exploited for switching, adding or dropping wavelength channels, or multiplexing operations. Such localized modes can also be the basis for wave length scale cavities and novel compact waveguide structures [47].

RESULTS AND DISCUSSION

The filling time, the time needs to flow liquid ^{4}He through the channels to fill the volume of exit reservoir with liquid ^{4}He. The filling time is predicted that follows the hyper-bola dependence, but it is obviously the experimental results shows that it did not follow the prediction of physical mechanism.

The volume flow rate of the liquid ^{4}He was experimentally calculated at the filling time, **t**, and constant volume of the exit reservoir (50 Nm^3/h).The volume flow rate $Q_{exp} = V = \pi r^2$, *unit cubic*. In order to explain the difficult question here, we divided the flow rate vs ΔP(ΔP=P_{in}-P_{out}) to two regimes:*regime I* (ΔP < 7 bars),and *regime II* (ΔP ≥ 7 bars).

It is clear that the *regime II*, which follows the *Heigen-Poiseuille* law, $Q_v = \frac{\pi r^4}{8\mu L}\Delta P$,the volume flowrate is well fitted to the linear dependence on ΔP, where rand L is a radius and a length of the channels, respectively, and μ is viscosity of liquid ^{4}He.

The *regime I*, the volume flow rate is non-linear dependence on ΔP and a laminar flow

regime. If one neglect the compressibility of liquid helium so the volume flow rate of liquid ^{4}He flow in the nanochannels can calculate by using the *Heigen-Poiseuille* equation.

The results show that the normalized coefficient, $C^* = \frac{Q_{exp}}{Q_{HP}}$, is a ratio between the experimental measurements volume flow rate and the theoretical values calculated. It obviously shows the absolute deviation between the experimental flow rate and the theoretical values, especially the regime I the C^* decreases sharply, in contract with it the regime II is very small change. The experimental results are higher than the theoretical values from 1 to 2 orders of magnitude.

There are several factors that may influence the experimental data with respect to the pressure drop: the deformation of the channels, the compressibility of the liquids, the slip and the viscosity.

They will be discussed in detail in the following. (1)Effect of the deformation of the channels: The channels constructed as a honeycomb structure with very thick walls as shown in the Figure 8b, on the other hand, the experiments was carried out at low temperature (≃2.4 K) so radius expansion of the channels can be neglected. (2)It is well known that the liquid helium can be compressed under a high pressure and *Mach number* may be served as a scale of the compressibility.

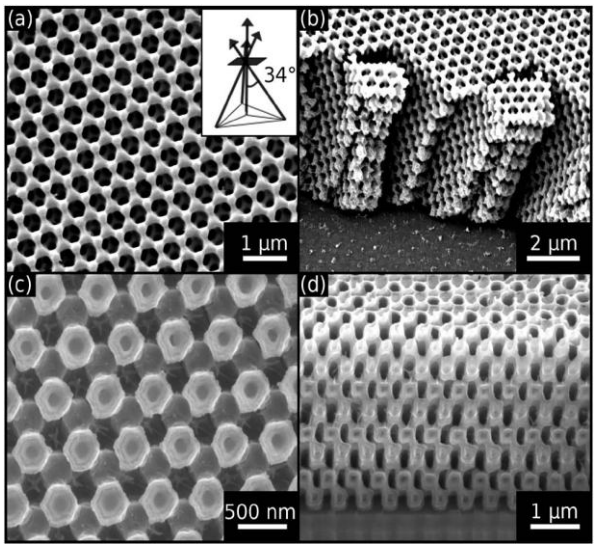

Fig. 8. Fourier transforms plots of typical waveforms for air, silicon, and photonic crystal samples

According to the relation of *Mach number*, $M_a = \frac{v_0}{v_s}$, where v_0 and v_s are velocity of liquid and sound in the liquid, respectively, and the density of the liquid helium, we have: $\frac{\Delta\rho}{\rho_0} = 2M_a^2$.

In the case of the maximum pressure of 25 bars and the maximum velocity of the liquid helium is 2.72 m/s, and *Mach number* is 0.4242. Therefore, we can obtain the relative change of the density, $\frac{\Delta\rho}{\rho_0} \gg 0.001\%$, which cannot be neglected. It obviously shows that the compressibility affects to the experimental results. However, the effect of the compressibility of liquid helium is not sufficient to explain the complicated dependence of the flow rate on the ΔP. (3) as the characteristic scale of the flow goes down to the micro/nanometer scale, the interaction between liquid and solid surface becomes more and more important. Considering the effect of the slip, a revised theoretical flow rate is obtained as $Q_{HP-slip} = v_s\frac{\pi R^2}{2} + \frac{\pi R^4 \Delta P}{8\mu L}$. The relative change of flowrate is defined as, $\frac{Q_{HP-slip}}{Q_{HP}} = (1 + \frac{4b}{R})$, where b is slip length and slip velocity, v_s, those values were calculated as following equations: $b = 0.059 \times \gamma^{0.485}$, and $v_s = b \times \gamma_{wall} = b \times \frac{R\Delta P}{2\mu_0 L}$. Note that the unit of slip length in the above equation is *nanometer*. In the case of the maximum applied pressure of 25 bars, the wall slip result is in about 2.6216times increase of flowrate. Thus, the effect of the wall slip is not sufficient to explain the increase of flowrate of liquid ^{4}He at the experimental conditions. In order to solve this problem we need to find the new model that can explain the complicated behavior of the flowrate on ΔP.

As mentioned in the experimental section, all the measurements were carried out at liquid helium temperature (≃2.4 K), at 1 bar, one needs take into account the effect of flow boiling in nanochannels. The nucleation criteria in narrow channels have been studied by a number of investigators, and it is generally believed that there are no significant differences from the conventional theories for large diameter tubes [48-50].

Small cavities on the channels wall trap helium vapor and serve as nucleation sites. As the channel wall temperature exceeds the saturation temperature, a bubble may grow inside the cavity

and appear at its mouth as show in Figure8. The formation of the nanobubbles on the channels wall and pressure driven flow forced liquid helium over it, the nanobubbles spread over the channel wall and become very thin helium gas coating surround the channel wall, so that the interface changes from liquid-solid to liquid-gas-solid. In the other word, the surface changes from hydrophilic to hydrophobic surface. Apparent viscosity of the liquid helium surround the channel decreased. It obviously is caused the flowrate anomalously increased in comparison with the HP model because the liquid helium can be slide over the surface channels wall like ice-skater. This can be explained very well why at the *regime I*, the flowrate increases non-linear and reach to saturation at certain pressure (may be at the critical pressure point at experiment temperature), at this pressure the flow boiling is suppressed (corresponding with 7 bar in the Figure 8)and reach to the transition point and change to the linear *regime II*.

For example, in the case of inlet pressure of 1.4bar (corresponding with ΔP = 0.4 bar in the Fig. 8), temperature ≃2.4K, if we choose typical values of the helium gas film, μ_g=1.2979×10^{-6}Pa.s, ρ=18.7 kg/m^3,and $v_z = 37.89$ m/s, the slip length of the gas layer [51] was calculated using the equation,$b = \frac{\mu}{\rho v_z} = 1.83$ μm,it is well agreement (experimental result is 2.16 μm) with the experimental results shown in Figure 8.

Thus, as gas film can indeed give a very large slip length. Our calculation assumed complete thermalization at each particle/boundary collision. If we have *nonzero reflectance* (especially on the solid wall), this would increase b even more, so that the experimental result as mentioned above is acceptable [52]. The discrepancy may be also caused by the effect of the compressibility of the helium liquid, temperature at the interface (channel wall-liquid helium) or something else in nanoscale that do not understand yet. When the inlet pressure applies higher but the temperature of the cell still keeps constant at ≃2.4 K, it means that the boiling conditions change, the boiling temperature increases with increasing pressure. In the *regime II*, the extrapolated of the fitted function at ΔP=0 but flowrate is nonzero, it means that the effects of the slip and flow boiling still remain affects.

CONCLUSIONS

A system for flow rate measurement of pressure driven flow in nano-channels was established. The mass flowrate of liquid ^{4}He as low as 10^{-12} kg/s (10^{-15} to 10^{-12} mol/s) was measured. For liquid helium flow in nanochannels, the gas thin film model is the good model to explain anomalously slip length or perfect slip effects were observed in the micro/nanoscale dimensions. The effective viscosity of the liquid helium was decreased by nanobubbles or nanogaseous films that were formed between liquid and the channel walls. These effects led anomalously increasing in transport properties of liquid helium in nanochannels. The conventional theories and/or Navier-Stokes equations could not be used to predict the flow in the nanochannels with small hydraulic diameters or flow at the closed boiling point. Finally, we note that the long wavelength (inset shows a schematic of the reflection geometry)(compared to visible and near-infrared optics) permits the easy fabrication of photonic crystals, which are essentially ideal, with no defects or disorder of any kind. As a result, these experiments are extremely well described by theoretical models, and it may be possible to observe subtle effects which would otherwise be obscured by the disorder present in less perfect samples.The cause of the discrepancy between the friction factor and location of the transition region was attributed to surface roughness.

However, amid all the investigations in mini- and microchannel flow, there seems to be a lack in the study of the flow in the transition region.

The major objectives of this research are accurately:

•Measure the pressure drop in micro-tubes;
•With almost the same diameter but;
•Different surface roughness and;
•Examine the effect of surface roughness;
•On the overall pressure drop characteristics and the start and end of the transition region.

The major objectives of this research are experimentally:

•Verified that the wrong selection of pressure sensing diaphragm lead to unrealistic results and frequently the unrealistic results were blamed to be the effect of roughness.

REFERENCES

[1] Ho C.M., TaiY.C., (1998), Micro-Electro-Mechanical-Systems. (MEMS) and fluid flows,*Annu. Rev. Fluid. Mech.* 30: 579-612.

[2] Craighead H.G., (2000), Nanoelectromechanical systems, *Science*. 290: 1532-1535.

[3] Giordano N., Cheng J.T. ,(2001), Microfluid mechanics: progress and opportunities,*J. Phys. Condens. Matter* .13:271–295

[4] Guo Z.Y., Li Z.X., (2003), Size effect on microscale single-phase flow and heat transfer, *Int. J. Heat Mass Transfer*.46: 149-159.

[5] Gad-el-Hak M., (2005), Liquids: The holy grail of microfluidic modeling Phys. Fluid 17 (1) 612-625.

[6] [6]. WhiteT.M., (2003), Fluids Mechanics, *McGraw-Hill, New York*.

[7] Yuqing Fu, Guoying Feng, Dayong Zhang, Jianguo Chen, Shouhuan Zhou,(2010), Beam quality factor of mixed modes emerging from a multimode step-index fiber, *Optik - International Journal for Light and Electron Optics*, 121(5) 452-456.

[8] Watanabe K., Udagawa Y., Udagawa H., (1999), Drag reduction of Newtonian fluid in a circular pipe with a highly water-repellent wall, *J Fluid Mech.* 381: 225–238

[9] Pit R., Hervet H., Leger L., (2000),Direct experimental evidence of slip inhexadecane:solid interfaces, *Phys. Rev. Lett*. 85: 980-983

[10] Baudry J., Charlaix E., Tonck A., Mazuyer D., (2001), Experimental evidence of a large slip effect at a nonwetting fluid–solid interface, *Langmuir*. 17: 5232–5236

[11] TrethewayD. C., Meinhart C. D., (2002), Apparent fluid slip at hydro- phoblic micro- channel walls, *Physics of Fluids*. 14: 9-12

[12] Zhu Y., Granick S., (2002), Limits of the Hydrodynamic No-Slip Boundary Condition, *Phys. Rev. Lett*. 88: 102-106

[13] Choi C.H., Westin K.J.A., Breuer K.S., (2003), Apparent Slip Flows in Hydrophilic and Hydrophobic Microchannels, *Physics of Fluids*. 15: 2897-2902

[14] Cottin-Bizonne C., Cross B., Steinberger A., Charlaix E., (2005), Boundary slip on smooth hydrophobic surfaces: Intrinsic effects and possible artifacts, *Phys. Rev.Lett*. 94: 056102

[15] Joseph P., Tabeling P., (2005), Direct measurement of the apparent slip length, *Phys. Rev. E*. 71: 035303

[16] Joly L., Ybert C., Bocquet L., (2006), Probing the Nanohydrodynamics at Liquid-Solid Interfaces Using Thermal Motion, *Phys. Rev. Lett*. 96: 046101

[17] Neto C., Evans D.R., Bonaccurso E., Butt H.J., Craig V.S.J., (2005), Boundary slip in Newtonian liquids: a review of experimental studies, *Rep. Prog. Phys*. 68: 2859-2897

[18] Thompson P.A., Robbins M.O., (1990), Shear flow near solids: epitaxial order and flow boundary conditions, *Phys. Rev*. 41: 6830-6837

[19] Sun M,.EbnerC., (1992), Molecular dynamics study of flow at a fluid-wall interface, *Phys. Rev. Lett*. 69: 3491-3494

[20] Koplik J., Banavar J.R., (1995),Continuum deductions from molecular hydrodynamics, *Annu. Rev. Fluid Mech*. 27: 257-292

[21] Barrat J.L., Bocquet L., (1999), Large slip effect at a nonwetting fluid-solid interface, *Phys. Rev. Lett*. 82: 4671-4674

[22] Cieplak M., Koplik J., Banavar J.R., (2001), Boundary conditions at a fluid–solid interface, Phys. *Rev. Lett*. 86: 803-806

[23] Nagayama G., Cheng P., (2004), Effects of interface wettability on microscale flow by molecular dynamics simulation, *Int. J. Heat Mass Transfer*. 47: 501-513

[24] Hendy S.C., Jasperse M., Burnell J., (2005), Effect of patterned slip on micro- and nanofluidic flows, *Phys. Rev.* 72:016303

[25] Voronov R.S., Lee L., (2006), Boundary slip and wetting properties of interfaces: correlation of the contact angle with the slip length, *J. Chem. Phys*. 124:204701

[26] Lichter S., Martini A., Snurr R.Q., Wang Q., (2007), Liquid Slip in Nanoscale Channels as a Rate Process, *Phys. Rev. Lett*. 98: 226001

[27] Tolstsoi, D.M., (1952). "Slip of Mercury on Glass", Dokl. Akad. Nauk SSSR 85, 1329-1335.

[28] Blake T.D., (1990), Slip between a liquid and a solid: D.M. Tolstoi's (1952) theory reconsidered, *Colloids Surf*. 47: 135–145

[29] Hocking L.M., (1976), A moving fluid on a rough surface. *J. Fluid Mech*. 76: 801-817

[30] Ponomarev I.V., Meyrovich A.E., (2003), *Phys. Rev*. 67: 26302

[31] Jabbarzadeh A., Atkinson J.D., Tanner I.R., (2000), Effect of wall roughness on slip and rheological properties hexadecance in molecular dynamics simulation of couette shear flow between two sinusoidal walls, *Phys. Rev*. 61: 690-699

[32] Vinogradova O.I., (1996), Hydrodynamic interaction of curved bodies allowing slip on their surfaces, *Langmuir*. 12: 5963-5968

[33] Thompson P.A., Troian S.M., (1997), A general boundary condition for liquid flow at solid surfaces, *Nature*. 389: 360-362

[34] Craig V.S.J., Neto C., Williams D.R.M., (2001), Shear Dependent Boundary Slip in an Aqueous Newtonian Fluid, *Phys. Rev. Lett*. 87: 54504-54507

[35] Zhu Y., Granick S., (2001), Rate-dependent slip of Newtonian liquid at smooth surfaces, *Phys. Rev. Lett*. 87: 96-105

[36] de Gennes P.G., (2002),On fluid/wall slippage, *Langmuir*. 18: 3413-3414

[37] Zhang X. H., Zhang X. D., Lou S.T., Zhang Z. X., Sun J. L., Hu J., (2004), Degassing and temperature effects on the information of nanobubbles at the mica/water interface, *Langmuir*. 20: 3813-3815

[38] Alexeyev A.A., Vinogradova O.I., (1996), Flow of a liquid in a nonuniformlyhydrophobized capillary, *Colloids Surf*. 108:173-179

[39] Borkent B.M., Dammer S.M., Schonherr H., Vansco G.J., Lohse D., (2007), Superstability of Surface Nanobubbles, *Phys. Rev. Lett*. 98: 204502

[40] Barthlott W., Neinhuis C., (1997), Purity of the sacred Lotus, or escape from contamination in biological surfaces, *Planta*. 202: 1-8

[41] Gao X.F., Jiang L., (2004), Water-repellent legs of water striders, *Nature (London).* 432: 36-36

[42] Galea T.M., Attard P., (2004), Constraint Method for Deriving Non-equilibrium ... the Fluid-Solid Boundary during Shear Flow, *Langmuir*. 20: 3477-3482

[43] Priezjev N.V., Darhuber A.A., Troian S.M., (2005), Slip behavior in liquid films on surfaces of patterned wettability: comparison between continuum and molecular dynamics simulations, *Phys. Rev*. 71: 041608

[44] Vonogradova O.I. Yakubov G.E., (2006), *Phys. Rev*. 73: 045302

[45] Yakovlev. D.G., Kaminker. A.D.,Gnedin. O.Y., Haensel. P., (2001), Neutrino emission from neutron stars, Physics Reports, 354(1–2):1-155.

[46] Nagarajan S., Yong Z., (2008), Use of Core/Shell Structured Nanoparticles for Biomedical Applications, *Biomedical Engineering*. 1: 34-42

[47] Bergles A.E., Rohsenow W.M., (1964), The Determination of Forced. Convection, Surface Boiling Heat Transfer, *J. Heat Trans*. 86: 365-372

[48] Sato T., Matsumura H., (1964), On the condition of incipient subcooled boiling with forced convection, *Bull. JSME*. 7(26): 392–398.
[49] David J.E. Anderson G.H., (1966), The incipience of nucleate boiling in forced convection flow, *AIChE J*. 12 (4): 774–780
[50] Kandlikar S.G., Mizo V.R., Cartwright M.D., Ikenze E., (1997),Bubble nucleation and growth characteristics in subcooled flow boiling of water, HTD-vol 342, *ASME Proceeding of 32nd National Heat Transfer Conference*. 4: 11-18
[51] Ishida N., Inoue T., Miyahara M., Higashitani K., (2000), Attraction between hydrophobic surfaces with and without gas phase, *Langmuir*. 16: 6377-6380
[52] Ghajar A.J., Tam L.M., Tam H.K., Wen Q., (2010),The Effect of Inner Surface Roughness on Friction Factor in Horizontal Micro-tubes, *Proceedings of 2nd International Conference on Mechanical and Electronics Engineering (ICMEE*). 1: 59-63.

Cite this article as: El-Sharkawy H. A.: Accurate characteristics of Helium in nano-channels. ***Int. J.Nano Dimens.*** 4(2): 117-129, Autumn 2013